# The first X-ray polarimetric observation of the black hole binary LMC X-1

J. Podgorný,[1,2,3]★ L. Marra,[4] F. Muleri,[5] N. Rodriguez Cavero,[6] A. Ratheesh,[5] M. Dovčiak,[2] R. Mikušincová,[4] M. Brigitte,[2] J. F. Steiner,[7] A. Veledina,[8,9] S. Bianchi,[4] H. Krawczynski,[6] J. Svoboda,[2] P. Kaaret,[10] G. Matt,[4] J. A. García,[11] P.-O. Petrucci,[12] A. Lutovinov,[13] A. Semena,[13] A. Di Marco,[5] M. Negro,[14,15] M. C. Weisskopf,[10] A. Ingram,[16] J. Poutanen,[8] B. Beheshtipour,[6] S. Chun,[6] K. Hu,[6] T. Mizuno,[17] Z. Sixuan,[17] F. Tombesi,[14,18,19] S. Zane,[20] I. Agudo,[21] L. A. Antonelli,[22,23] M. Bachetti,[24] L. Baldini,[25,26] W. H. Baumgartner,[10] R. Bellazzini,[25] S. D. Bongiorno,[10] R. Bonino,[27,28] A. Brez,[25] N. Bucciantini,[29,30,31] F. Capitanio,[5] S. Castellano,[25] E. Cavazzuti,[32] C. Chen,[33] S. Ciprini,[19,23] E. Costa,[5] A. De Rosa,[5] E. Del Monte,[5] L. Di Gesu,[32] N. Di Lalla,[34] I. Donnarumma,[32] V. Doroshenko,[35] S. R. Ehlert,[10] T. Enoto,[36] Y. Evangelista,[5] S. Fabiani,[5] R. Ferrazzoli,[5] S. Gunji,[37] K. Hayashida,[38] J. Heyl,[39] W. Iwakiri,[40] S. G. Jorstad,[41,42] V. Karas,[2] F. Kislat,[43] T. Kitaguchi,[36] J. J. Kolodziejczak,[10] F. La Monaca,[5] L. Latronico,[27] I. Liodakis,[44] S. Maldera,[27] A. Manfreda,[45] F. Marin,[1] A. Marinucci,[32] A. P. Marscher,[41] H. L. Marshall,[46] F. Massaro,[27,28] I. Mitsuishi,[47] C.-Y. Ng,[48] S. L. O'Dell,[10] N. Omodei,[34] C. Oppedisano,[27] A. Papitto,[22] G. G. Pavlov,[49] A. L. Peirson,[34] M. Perri,[22,23] M. Pesce-Rollins,[25] M. Pilia,[24] A. Possenti,[24] S. Puccetti,[23] B. D. Ramsey,[10] J. Rankin,[5] O. J. Roberts,[33] R. W. Romani,[34] C. Sgrò,[25] P. Slane,[7] P. Soffitta,[5] G. Spandre,[25] D. A. Swartz,[33] T. Tamagawa,[36] F. Tavecchio,[50] R. Taverna,[51] Y. Tawara,[47] A. F. Tennant,[10] N. E. Thomas,[10] A. Trois,[24] S. S. Tsygankov,[8] R. Turolla,[20,51] J. Vink,[52] K. Wu[20] and F. Xie[53,5]

*Affiliations are listed at the end of the paper.*

Accepted XXX. Received YYY; in original form ZZZ



**ABSTRACT**

We report on an X-ray polarimetric observation of the high-mass X-ray binary LMC X-1 in the high/soft state, obtained by the *Imaging X-ray Polarimetry Explorer* (*IXPE*) in October 2022. The measured polarization is below the minimum detectable polarization of 1.1 per cent (at the 99 per cent confidence level). Simultaneously, the source was observed with the *NICER*, *NuSTAR* and *SRG*/ART-XC instruments, which enabled spectral decomposition into a dominant thermal component and a Comptonized one. The low 2–8 keV polarization of the source did not allow for strong constraints on the black-hole spin and inclination of the accretion disc. However, if the orbital inclination of about 36 degrees is assumed, then the upper limit is consistent with predictions for pure thermal emission from geometrically thin and optically thick discs. Assuming the polarization degree of the Comptonization component to be 0, 4, or 10 per cent, and oriented perpendicular to the polarization of the disc emission (in turn assumed to be perpendicular to the large scale ionization cone detected in the optical and radio bands), an upper limit to the polarization of the disc emission of 0.5, 1.7, or 3.6 per cent, respectively, is found (at the 99 per cent confidence level).

**Key words:** accretion, accretion discs – black hole physics – polarization – scattering – X-rays: binaries – X-rays: individual: LMC X-1

## 1 INTRODUCTION

LMC X-1 is the first discovered extragalactic black-hole X-ray binary system (Mark et al. 1969). Being located in the Large Magellanic Cloud, the source has a well determined distance of 48 ± 2 kpc with low absorption along the line of sight (Orosz et al. 2007, 2009; Hanke et al. 2010). LMC X-1 is persistent and bright; hence, it has been studied extensively since its discovery. X-ray binary systems typically exhibit two distinct spectral states in the X-ray band: the 'high/soft state' in which the thermal emission from a multi-temperature black-

★ E-mail: jakub.podgorny@astro.unistra.fr

body accretion disc (Shakura & Sunyaev 1973; Novikov & Thorne 1973) is dominant and the 'low/hard state' in which a power-law component is dominant (Zdziarski & Gierliński 2004; Remillard & McClintock 2006). While many X-ray binary systems change their spectral state over time, LMC X-1 has always been observed in the soft state with $L_X \sim 2 \times 10^{38}$ erg s$^{-1}$ (Nowak et al. 2001; Wilms et al. 2001). Typically more than 80 per cent of the X-ray flux can be attributed to the thermal/disc component (see e.g. Nowak et al. 2001; Steiner et al. 2012; Bhuvana et al. 2021; Jana et al. 2021; Bhuvana et al. 2022). The remainder of the X-ray flux can be decomposed into coronal power-law emission (Sunyaev & Titarchuk 1980), a broad Fe-line from the relativistic disc (Fabian et al. 1989), and a narrow Fe-line that most likely originates from scattering off highly ionized wind from the stellar companion (Steiner et al. 2012).

Optical and near-infrared observations reveal an O7/O9 giant donor with a mass of $M_2 = 31.8 \pm 3.5\,M_\odot$ (Orosz et al. 2009). The same dynamical study confirms a black-hole accretor with a mass of $M_{BH} = 10.9 \pm 1.4\,M_\odot$ and an orbital inclination $i = 36.4° \pm 1.9°$. The measured orbital period of LMC X-1 is $3.90917 \pm 0.00005$ days (Orosz et al. 2009), based on high-resolution optical spectroscopy. Over an orbit, the X-ray flux exhibits achromatic sinusoidal amplitude variations of 7 per cent associated with the inferior/superior conjunctions and Thomson scattering by the stellar wind (Nowak et al. 2001; Orosz et al. 2009; Hanke et al. 2010). Strong red noise variability is observed on timescales shorter than the orbital period (Schmidtke et al. 1999; Nowak et al. 2001; Bhuvana et al. 2022). Also, low frequency quasi-periodic oscillations (QPOs) were observed on several occasions (Ebisawa et al. 1989; Alam et al. 2014), which do not fit well within the standard low-frequency QPO ABC classification (Casella et al. 2005).

Measurement of the spin of the BH in LMC X-1 is of great interest. The system is a high-mass X-ray binary, and estimation of the black-hole spin is useful for stellar evolution and cosmological studies (see e.g. Qin et al. 2019; Mehta et al. 2021). The donor star is 5 Myr past the zero-age main sequence and believed to be filling 90 per cent of its Roche lobe. This, and the inferred dynamical parameters of the system, suggest that LMC X-1 is likely a precursor of an unstable mass transfer phase and a common-envelope merger (Podsiadlowski et al. 2003; Orosz et al. 2009; Belczynski et al. 2012). Such systems are of potential interest for gravitational-wave studies, especially regarding the spin of the black hole (BH) (Belczynski et al. 2021; Fishbach & Kalogera 2022; Shao & Li 2022). Many spectroscopic studies have estimated the spin of the BH in LMC X-1, using the continuum and relativistic line fitting techniques in Kerr spacetime, assuming the spin is aligned with the system axis of symmetry (see Tripathi et al. 2020, for LMC X-1 studies beyond the Kerr metric). They infer remarkably high spin values: $0.85 \lesssim a \lesssim 0.95$ (continuum method; Gou et al. 2009; Mudambi et al. 2020; Jana et al. 2021; Bhuvana et al. 2022) and $0.93 \lesssim a \lesssim 0.97$ (Fe-line method; Steiner et al. 2012; Bhuvana et al. 2022). Along with the high spin, high accretion rates of $0.07 \lesssim \dot{M}/\dot{M}_{Edd} \lesssim 0.24$ and luminosities $0.1 \lesssim L_X/L_{Edd} \lesssim 0.16$ are estimated (the quantities are defined in Bhuvana et al. 2022). The power-law index tends to be steep $2 \lesssim \Gamma \lesssim 4$ (Gou et al. 2009; Jana et al. 2021; Bhuvana et al. 2022; Nowak et al. 2001). A counter-argument to the high spin of LMC X-1 through X-ray spectroscopy was given by Koyama et al. (2015) that introduced a double Compton component model to fit the data, which allows a larger disc inner radius, leading to a lower spin estimate.

X-ray polarimetry can constrain the geometry of the unresolved inner accretion flow and the inclination of the accretion disc with respect to the observer. It can also independently constrain the spin of the BH (Connors & Stark 1977; Stark & Connors 1977; Connors et al. 1980; Dovčiak et al. 2004, 2008; Li et al. 2009; Schnittman & Krolik 2009, 2010; Cheng et al. 2016; Taverna et al. 2020; Taverna et al. 2021; Krawczynski & Beheshtipour 2022), especially in the high/soft state when the accretion disc is widely believed to extend to the inner-most stable circular orbit.

We present the first X-ray polarimetric measurement of LMC X-1, which serves as an example of an accreting BH caught in the thermal state. The *Imaging X-ray Polarimetry Explorer* (*IXPE*) (Weisskopf et al. 2022) observed LMC X-1 in the 2–8 keV band in which the disc emission dominates during October 2022. Simultaneous X-ray observations were performed with the *NICER* (Gendreau et al. 2012), *NuSTAR* (Harrison et al. 2013) and ART-XC (Pavlinsky et al. 2021) instruments to better characterize the source spectrum. The *IXPE* observation of LMC X-1 helps fill out the sample of accreting BHs with X-ray polarization measurements which includes the accreting stellar-mass BHs in Cyg X-1 (Krawczynski et al. 2022) and Cyg X-3 (Veledina et al. 2023) (in the low/hard or intermediate states), and the supermassive BHs in MCG 05-23-16 (Marinucci et al. 2022) and the Circinus galaxy (Ursini et al. 2023). We obtained a low upper limit on the 2–8 keV polarization of LMC X-1 in the thermal state. Our careful spectro-polarimetric analysis leads to constraints on polarization of the distinct X-ray spectral components and validates long-standing theoretical predictions for X-ray properties of the inner-most regions of accreting BHs.

Independent constraints on the accretion disc orientation are important when interpreting the X-ray polarization results. A $\sim$ 15 pc parabolic structure in the form of a surrounding nebula (wind or jet powered) was detected in both optical and radio observations (Pakull & Angebault 1986; Cooke et al. 2008; Hyde et al. 2017). The nebula is aligned with an inner $\sim$ 3.8 pc ionization cone of 45° opening angle seen in He II and [O III] lines, which is believed to be directly related to the BH accreting structure (Cooke et al. 2007; Cooke et al. 2008). We use this large-scale measurement of the disc orientation to assess the X-ray polarization position angle measured by *IXPE* at sub-pc scales; this is similar to comparison made for Cyg X-1 (Krawczynski et al. 2022). The jet of LMC X-1 has not been detected yet (Fender 2006; Hughes et al. 2007; Hyde et al. 2017) and is likely to be switched-off since the binary is persistently in the thermal state (Cooke et al. 2007).

The paper is organized as follows. Section 2 describes the observations and the data reduction techniques. Our spectral and polarimetric results are presented in Section 3. Sections 4 and 5 provide an interpretation of the results and a summary.

## 2 OBSERVATIONS AND DATA REDUCTION

*IXPE* (Weisskopf et al. 2022) observed LMC X-1 between 2022 Oct 19 15:01:48 UTC and 2022 Oct 28 04:39:09 UTC, under the observation ID 02001901 and for a total lifetime of $\sim$ 562 ks for each of its three telescopes. Processed, Level 2, data already suitable for scientific data analysis were downloaded from the *IXPE* HEASARC archive.[1] Source and background regions were spatially selected in the *IXPE* field of view defining different concentric regions, both centered on the image barycenter. The source region is defined as a circle with radius 1.5 arcmin, while the background region is an annulus with inner and outer radii of 2.5 and 4 arcmin, respectively. We show these regions on top of the *IXPE* count maps in Appendix A.

[1] Available at https://heasarc.gsfc.nasa.gov/docs/ixpe/archive/.

Two different approaches were used to estimate the X-ray polarization. The first relies on the use of forward-folding fitting software (we used XSPEC, Arnaud 1996, version 12.13.0) to model Stokes spectra $I$, $Q$ and $U$. This allows us to model the spectrum of the source $I$ with different components, associating to each of them a polarization model which is constrained using the $Q$ and $U$ spectra. An alternative approach makes use of the IXPEOBSSIM package (Baldini et al. 2022), which provides tools for *IXPE* data analysis including the `PCUBE` algorithm of the `xpbin` function, which calculates the polarization degree and angle from the Stokes parameters without making any assumption on the emission spectrum. For XSPEC analysis, we used the formalism from Strohmayer (2017) and used the weighted analysis method presented in Di Marco et al. (2022) (parameter stokes=Neff in `xselect`).

The polarization cubes (PCUBEs) for both the source and background regions generated with IXPEOBSSIM combine the observations from each detector unit (DU), and return the total polarization degree and angle as well as the minimum detectable polarization (MDP) at 99 per cent confidence level. Using `xpbin` with the `PHA1, PHA1Q, PHA1U` algorithms, we created spectral files of Stokes $I$, $Q$ and $U$ parameters, respectively. These files are produced in the OGIP, type 1 PHA format, which is convenient for spectral, polarimetric, and joint analysis within XSPEC.

Appendix A contains a full description of the *NICER*, *NuSTAR* and ART-XC observations and the data reduction. This includes discussion of our use of the cross-calibration model `MBPO` employed to reconcile discrepancies between the instruments and of level of the systematic uncertainties of the instruments.

## 3 DATA ANALYSIS

### 3.1 Spectral and timing analysis

Daily monitoring by the Gas Slit Camera (GSC) onboard of MAXI (Matsuoka et al. 2009) confirmed that during our observations, there were no outbursts or long-term flux variations that would suggest that the source departed from the high/soft state. In this study, we analyzed in more detail the flux variability of LMC X-1 during the *IXPE* observation, using light curves from the simultaneous observations by *NICER*, *NuSTAR* and ART-XC (see Fig. 1). We used the following energy ranges for the light curves: 0.3–12 keV, 3–18 keV and 4–12 keV, respectively for *NICER*, *NuSTAR* and ART-XC. The corresponding time bins were 920 s for *NICER*, 400 s for *NuSTAR* and ART-XC, and 1000 s for *IXPE*.

The *IXPE* and *NICER* observations cover a period of 10 days, while *NuSTAR* and ART-XC complement these observations with snapshots in the hard X-ray band. Our *IXPE* and *NICER* observations thus include about two and half orbits ($P$ = 3.90917 days) of the black hole and companion star. Orosz et al. (2009) measured orbital variations of the X-ray flux to be consistent with the periodicity measured from optical data. The X-ray orbital variability was revealed via a set of *RXTE*/ASM (Levine et al. 1996) data from over 12 years monitoring, and it was attributed to the electron scattering in the stellar wind from the companion star (Orosz et al. 2009; Levine et al. 2011). To estimate the X-ray flux orbital variations in the current observations, we took the orbital ephemeris from the 'adopted' model in table 3 of Orosz et al. (2009); in particular, we assumed an orbital period of 3.90917 days and a time of the inferior conjunction of 53390.8436 MJD (Modified Julian Date). We took the parameters of the best-fitting sinusoidal curve from their table 1 for the 1.5–12 keV energy band, where they had parameters averaged

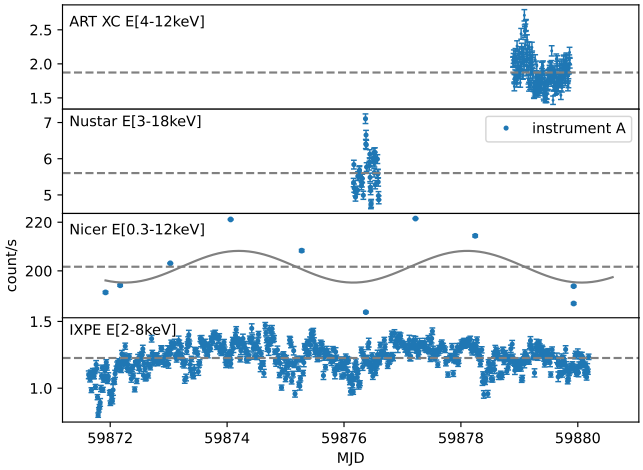


**Figure 1.** X-ray light curves of LMC X-1. *Top panel*: ART-XC light curve for the energy range 4–12 keV. *Second panel*: *NuSTAR* light curve for the energy range 3–18 keV from the instrument A of *NuSTAR*. *Third panel*: *NICER* light curve for the energy range 0.3–12 keV with a sinusoidal curve showing the expected orbital variations of the X-ray flux based on previous *RXTE* monitoring of the source. *Bottom panel*: *IXPE* light curve for the energy range 2–8 keV. The dashed horizontal lines are the average count rate for each light curve.

over the 12 years observation with *RXTE*, and we rescaled to the *NICER* count rate. The *NICER* count rate versus orbital phase is then $f(\phi) = a_0 + a_1 \cos(2\pi\phi)$ where $a_0 = 201.69$, $a_1 = 6.51$, and $\phi$ the phase. The curve is shown along with *NICER* data in the third panel of Fig. 1. Comparison of the curve and the data indicates that the X-ray variations in the *NICER* light curve can be well explained by the expected orbital variations. Similar variations are apparent in the *IXPE* light curve. The X-ray flux minima correspond to inferior conjunctions of the secondary star that are associated with the enhanced absorption of the black-hole accretion-disc X-ray emission due to the wind from the companion.

In the light curves acquired in the hard X-ray band (ART-XC and *NuSTAR*), stochastic noise dominates over the orbital variations. Similar to previous research (see Koyama et al. 2015), we observe an increase in stochastic red noise variability with energy. The power spectrum in the hard band can be described with a power law with index $\approx -1$ and normalization consistent with the previous measurements (see e.g. Bhuvana et al. 2021). No obvious QPOs were observed in the power spectrum. It should be noted, that low frequency QPOs were previously observed in this system during short episodes of spectral hardening within the soft state (Ebisawa et al. 1989; Alam et al. 2014).

Using the *NICER* and *NuSTAR* spectral data, we calculated the hardness ratio defined as the ratio between the flux in the hard band and the total flux. We defined the soft vs. hard bands to be 0.3–3 keV vs. 3–12 keV for *NICER*, and 3–8 keV vs. 8–20 keV for *NuSTAR*. In Fig. 2, we show the evolution of the hardness ratio for the *NICER* and *NuSTAR* data. The *NICER* hardness ratio is consistent with being constant with a hardness of 0.006 within the measurement uncertainties. The low hardness indicates that the source is in the soft state when the accretion-disc thermal emission clearly dominates in the X-ray spectrum. The *NuSTAR* hardness ratio is $0.022 \pm 0.005$ for the simultaneous observation with *IXPE*.

Because the spectral hardness appears constant over the observations, and given the stability in flux, we used *NICER*, *NuSTAR*,

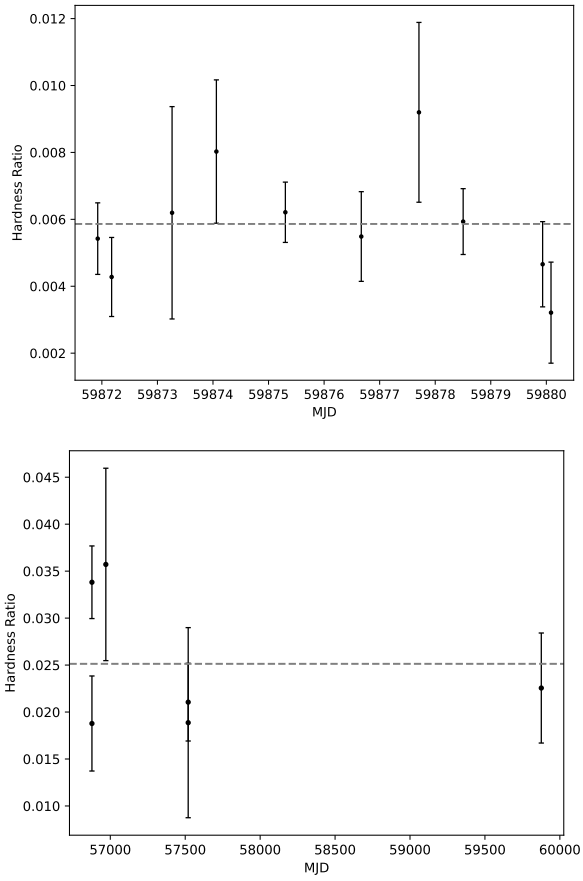


**Figure 2.** Time variation of X-ray hardness ratios. *Top panel*: Ratio of the *NICER* count rates in the hard (3–12 keV) and the soft (0.3–3 keV) bands. *Bottom panel*: Ratio of the *NuSTAR* count rates in the hard (8–20 keV) and the soft (3–8 keV) bands.

and *IXPE* time-averaged spectra for the spectral fitting. We used the XSPEC package and employed the following model for the time-averaged analysis:

$$\texttt{GABS} \times \texttt{TBFEO}\,(\texttt{GAUSSIAN} + \texttt{KERRBB} + \texttt{NTHCOMP}). \quad (1)$$

We used KERRBB (Li et al. 2005) to model general relativistic accretion disc emission from a multi-temperature blackbody and NTHCOMP (Zdziarski et al. 1996; Życki et al. 1999) for the thermally Comptonized continuum. For the KERRBB model, we kept the black-hole mass and distance fixed at the values reported for the source, ($M_{\rm BH}$ = 10.9 $M_\odot$, $d$ = 48.1 kpc Orosz et al. 2009; Hanke et al. 2010) and assumed the disc axis to be aligned with the binary system orbital inclination ($i$ = 36.4° Orosz et al. 2009), i.e. the disc is not warped. We fixed the dimensionless spin parameter of the black hole to the best-fitting value of 0.92 found with the continuum fitting method by Gou et al. (2009). We also kept the spectral hardening factor fixed at 1.7, and assumed no torque at the inner disc edge.

The blackbody seed photon temperature $kT_{\rm bb}$ of the NTHCOMP model is 0.3969 ± 0.0085 keV, slightly lower than those reported in Gierliński et al. (2001), Kubota et al. (2005) and Gou et al. (2009). But it was obtained from prior modeling where $kT_{\rm bb}$ was tied to the $kT_{\rm in}$ of the multi-blackbody model DISKBB to calculate the temperature of the inner edge of the accretion disc and the Compton up-scattering of seed photons at this temperature. The *int_type* parameter of NTHCOMP is set to 0 for blackbody seed photons.

A GAUSSIAN component was added at 0.866 keV with a line width

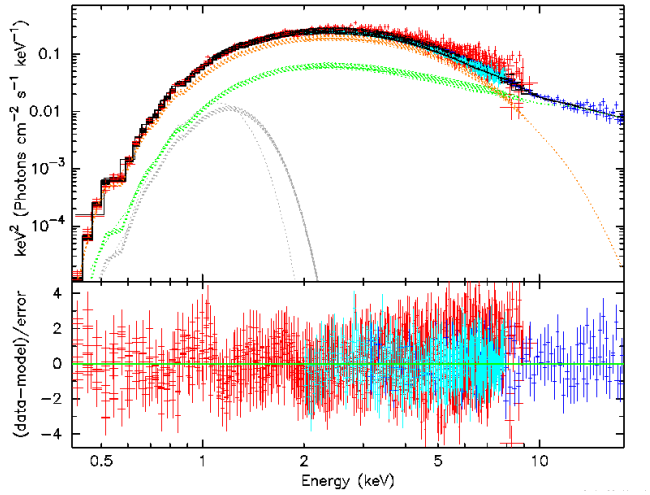


**Figure 3.** X-ray spectra of LMC X-1. *Top panel*: *NICER* (red), *NuSTAR* (blue), and *IXPE* (cyan) spectra unfolded around the best-fitting model described by Model 1 in $EF(E)$ space. The total model for each data set is shown in black with individual GAUSSIAN, KERRBB, and NTHCOMP contributions in light gray, orange, and green, respectively. *Bottom panel*: Model-data deviations (residuals) in $\sigma$.

of 0.307 keV to account for an emission feature that resembles the first-order scattering of anisotropic photons onto isotropic electrons like that in Zhang et al. (2019), figure 8. *NICER* observation 3 presented a narrower GAUSSIAN component that required different line width and normalization parameter values with the line energy consistent to other *NICER* observations within the 90 per cent confidence interval. GABS was used to model a broad Gaussian-like absorption artifact at 9.78 ± 0.26 keV detected with *NuSTAR* that may be due to Comptonization in the upper layers of the disc not being modeled properly, an inhomogeneous corona, a broad instrumental absorption feature, or an unmodelled weak reflection component. The line energies for both of the identified emission and absorption-like features, $E_{\rm l}$ in GAUSSIAN and GABS respectively, are left frozen while their line widths and normalization/depth are allowed to vary freely.

TBFEO (Wilms et al. 2000) was used to account for the X-ray absorption in the interstellar medium by hydrogen, oxygen, and iron. The iron abundance relative to Solar, Fe in TBFEO, is fitted to 0.69 ± 0.13 without allowing it to go to a higher abundance than oxygen.

We find the best-fitting model has $\chi^2/{\rm dof} = 3438.53/2570$. We estimate a black-hole accretion rate of $\dot{M} = (1.568\pm0.015)\times10^{18}$ g s$^{-1}$, consistent with values previously reported for the source (Gou et al. 2009; Jana et al. 2021). The flux in the 2–8 keV energy range is dominated by the accretion disc emission with KERRBB contributing 74.54 per cent, while the coronal emission (NTHCOMP) contributes 25.45 per cent. Figure 3 shows the unfolded spectra and the best-fitting parameters as reported in Table 1.

The obtained $\chi^2/{\rm dof}$ for the best-fitting model is greater than 1, despite the addition of systematic errors (see Appendix A). This may be due to several reasons: cross-calibration uncertainties between the different instruments, short term source variability, different exposure intervals of the various satellites, and complexity of the X-ray spectra of Galactic BHs which may be not fully captured by the model. However, as a detailed spectral analysis is beyond the scope of the paper and a visual inspection of the residuals seems to indicate that the global fit is not obviously incorrect, we used the best-fitting model to derive the polarization properties of the various spectral components.

| Component | Parameter (unit) | Description | Value |
|---|---|---|---|
| TBFEO | $N_{\rm H}$ ($10^{22}$ cm$^{-2}$) | Hydrogen column density | $0.890^{+0.012}_{-0.017}$ |
| | O | Oxygen abundance | $0.866^{+0.033}_{-0.037}$ |
| | Fe | Iron abundance | $0.69^{+0.13}_{-0.12}$ |
| | $z$ | Redshift | 0.0 (frozen) |
| KERRBB | $\eta$ | Inner-edge torque | 0.0 (frozen) |
| | $a$ | Black-hole spin | 0.92 (frozen) |
| | $i$ (deg) | Inclination | 36.4 (frozen) |
| | $M_{\rm bh}$ ($M_\odot$) | Black-hole mass | 10.9 (frozen) |
| | $M_{\rm dd}$ ($10^{18}$ g s$^{-1}$) | Mass accretion rate | $1.568^{+0.015}_{-0.014}$ |
| | $D_{\rm bh}$ (kpc) | Distance | 48.1 (frozen) |
| | $hd$ | Hardening factor | 1.7 (frozen) |
| | $r_{\rm flag}$ | Self-irradiation | 1 (frozen) |
| | $l_{\rm flag}$ | Limb-darkening | 0 (frozen) |
| | norm | Normalization | $0.739^{+0.005}_{-0.005}$ |
| NTHCOMP | $\Gamma$ | Photon index | $3.19^{+0.04}_{-0.05}$ |
| | $kT_{\rm e}$ (keV) | Electron temperature | 100.00 (frozen) |
| | $kT_{\rm bb}$ (keV) | Seed photon temperature | $0.397^{+0.009}_{-0.008}$ |
| | norm ($10^{-2}$) | Normalization | $4.19^{+0.16}_{-0.16}$ |
| GAUSSIAN | $E_{\rm l}$ (keV) | Line energy | $0.866^{+0.019}_{-0.019}$ |
| | $\sigma$ (keV) | Line width | $0.307^{+0.016}_{-0.016}$ |
| | norm ($10^{-2}$ photons cm$^{-2}$ s$^{-1}$) | Normalization | $2.39^{+0.19}_{-0.20}$ |
| GABS | $E_{\rm l}$ (keV) | Line energy | $9.78^{+0.26}_{-0.24}$ |
| | $\sigma$ (keV) | Line width | $1.17^{+0.23}_{-0.21}$ |
| | Strength (keV) | Line depth | $0.48^{+0.12}_{-0.12}$ |

**Table 1.** Best-fitting parameters (with uncertainties at 90 per cent confidence level) of the joint *NICER*, *NuSTAR*, and *IXPE* spectral modeling with the combined model described by Model 1. GAUSSIAN parameter values for the *NICER* observation 3 are: $E_{\rm l} = 0.872 \pm 0.012$ keV, $\sigma = 0.2311 \pm 0.0089$ keV, norm = $0.0337 \pm 0.0015$ photons cm$^{-2}$ s$^{-1}$. See Appendix A for discussion of the normalization of the KERRBB component.

### 3.2 Polarimetric analysis with PCUBEs

We show in Fig. 4 the normalized Stokes parameters ($Q/I$ and $U/I$) for a single energy bin 2–8 keV, for each DU separately, and summed. The polarization angle measured by *IXPE* using the sum of all three DUs is $51.6° \pm 11.8°$ in the north-east direction and the polarization degree is $1.0 \pm 0.4$ per cent. Given this measurement, we have a $3\sigma$ upper limit on polarization degree of 2.2 per cent. The polarization angle value is roughly aligned with the ionization cone structure detected in He II $\lambda$4686/H$\beta$ and [O III] $\lambda$5007/H$\beta$ line ratio maps at 225° north-east (with an opening angle of 45°) (Cooke et al. 2007; Cooke et al. 2008). The obtained low value of the upper limit on the polarization degree is consistent with the analytical prediction given by Chandrasekhar's formulae (Chandrasekhar 1960) for scattering-induced polarization of pure thermal emission in semi-infinite disc atmospheres seen at inclination below $\sim 60°$. However, see Section 3.3 for a careful discussion of the polarization result with respect to the two observed spectral components. The MDP at 99 per cent confidence level in 2–8 keV is 1.1 per cent, which means the obtained polarization result is not statistically significant. Reducing the energy range does not improve the statistical significance.

Although no average polarization is observed, a *time-dependent* signal may still be present in the *IXPE* observation. To check for this possibility, we adopted the the dedicated IXPEOBSSIM function to calculate the normalized Stokes parameters $Q/I$ and $U/I$ in time bins of 30 ks (see Fig. 5). These can be considered independent normal variables (Kislat et al. 2015) and we fit their values as a function of time with a constant line. The fit null probability, which expresses the probability that the observed variations around the model are due to chance alone, is $\approx$ 50 per cent for both $Q/I$ and $U/I$ for the value of the $\chi^2$ found and the number of degrees of freedom of the fit. Then, we derived that any observed variability of polarization is compatible with statistical fluctuations only.

We repeated a similar procedure to investigate possible dependence of polarization on the orbital phase. We first derived the phase of each event from its arrival time using the orbital ephemeris described in Section 3.1. Then, we folded the events into 7 phase bins. When only the events in the 2–4 keV energy range are selected for

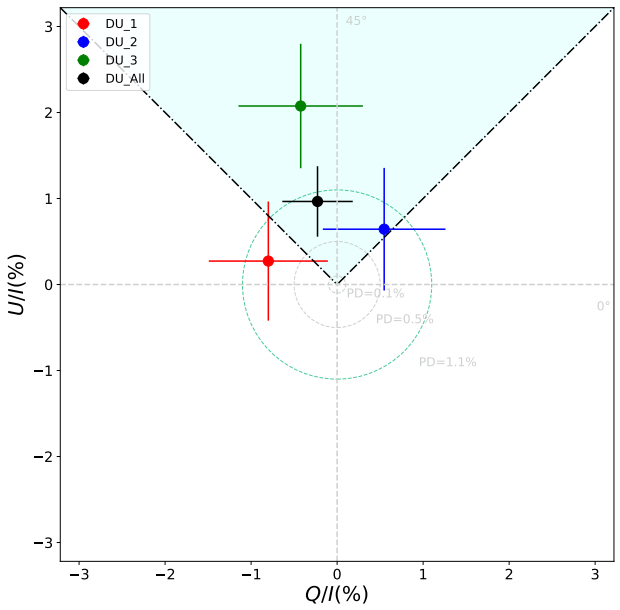


**Figure 4.** Normalized $Q/I$ and $U/I$ Stokes parameters and corresponding polarization degree and angle for DU1 (red), DU2 (green), DU3 (blue) and a sum of the three units (black). The (light green) circle represents the MDP value at the 99 per cent confidence level and the cyan-shaded area the direction and opening angle of the ionization cone (Cooke et al. 2008). The data are obtained using a single energy bin in the 2–8 keV energy band. We report the uncertainties at $1\sigma$ level, i.e. at the 68.3 per cent confidence.

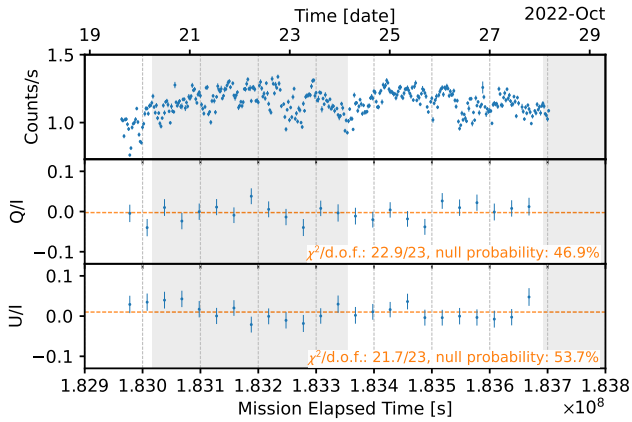


**Figure 5.** Counting rate (*top*) and normalized Stokes $Q$ and $U$ parameters (*middle* and *bottom*, respectively) measured by *IXPE* as a function of time. Time bin is 2 ks for counting rate and 30 ks for $Q$ and $U$. Horizontal, dashed lines are the best fit with a constant line: the obtained $\chi^2$, the number of degrees of freedom and the corresponding null probability are indicated. The gray-shaded and white regions identify subsequent orbits of LMC X-1.

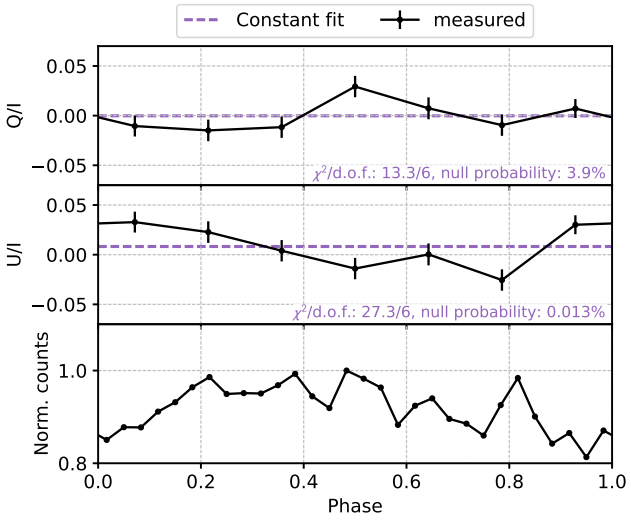


**Figure 6.** Variation of the normalized Stokes parameters $Q$ (*top*) and $U$ (*middle*), calculated with IXPEOBSSIM, as a function of the orbital phase of LMC X-1. As in Fig. 5, horizontal, dashed lines are the best fit with a constant line, and the $\chi^2$, the number of degrees of freedom and the corresponding null probability of the fit are indicated. The corresponding normalized flux from *IXPE* (*bottom*) as a function of the orbital phase is added for comparison.

| Component | Parameter (unit) | Description | Value |
|---|---|---|---|
| POLCONST (1) | $\Pi$ (%) | Polarization degree | $\leq 8$ |
| | $\Psi$ (deg) | Polarization angle | Unconstrained |
| POLCONST (2) | $\Pi$ (%) | Polarization degree | $\leq 46$ |
| | $\Psi$ (deg) | Polarization angle | Unconstrained |
| KYNBBRR | arate ($\dot{M}_{\rm Edd}$) | Mass accretion rate | $0.168^{+0.003}_{-0.003}$ |
| | norm ($10^{-2}$) | Normalization | $3.93^{+0.08}_{-0.08}$ |
| | $\chi$ (deg) | disc axis orientation | Unconstrained |
| POLCONST (3) | $\Pi$ (%) | Polarization degree | $\leq 8.6$ |
| | $\Psi$ (deg) | Polarization angle | Unconstrained |

**Table 2.** Best-fit parameters of the *IXPE* polarimetric analysis described in Section 3.3. The components POLCONST (1) and (2) are used to model the polarization properties of the disc and the corona emission, respectively, as described in Section 3.3.1. Meanwhile the component POLCONST (3) is used to describe the coronal emission polarization properties in the model described in Section 3.3.2.

the analysis, a fit with a constant is not acceptable, especially for $U/I$ (see Fig. 6). Summing the $\chi^2$ values obtained for the fit of both the Stokes parameters and, correspondingly, their degrees of freedom, the null probability of the combined fit is 0.0057 per cent. This further supports the fact that the emission from LMC X-1 may indeed be polarized at a few per cent, but its polarization angle, degree, or both, could depend on the orbital phase. When summing over time scales comparable to the orbital period, an orbital-phase-dependent polarization would be averaged to a low value that would be undetected in the phase-average analysis. However, *IXPE* observed only two complete orbits of LMC X-1 (see Fig. 5); therefore further observations would be needed to detect orbital-phase-dependent polarization with high statistical confidence.

### 3.3 Polarimetric analysis with XSPEC

#### *3.3.1 Phenomenological polarization model*

For the polarimetric fit of our data, we removed the *NICER* and *NuSTAR* spectra and included the *IXPE* $Q$ and $U$ spectra. Since our aim here was to explore the polarimetric properties of the source with the simplest possible model, we removed both GAUSS and GABS component from Model 1 and we convolved the thermal and the comptonized components with the polarization model POLCONST; this is characterized by two parameters, the polarization degree $\Pi$ and angle $\Psi$, both constant with energy. Thus the model employed in the fitting procedure is as follows:

$$\texttt{TBFEO} * (\texttt{POLCONST} * \texttt{KERRBB} + \texttt{POLCONST} * \texttt{NTHCOMP}) \quad (2)$$

We obtained the best-fitting $\chi^2/\mathrm{dof} = 1492.31/1341$, with the polarization parameters values listed in Table 2.

Because we obtained only an upper limit on the polarization degree, we were not able to constrain the polarization properties of both spectral components at the same time. Thus we decided to further analyze the polarimetric data by tying the two components' polarization angles. In particular the polarization degree and angle associated with the accretion disc thermal emission were left free to vary, while we linked the polarization angle of the coronal emission to that of the thermal emission. Because of the symmetry of the system, the polarization vector of the thermal emission is expected to be either parallel or perpendicular to the disc symmetry axis. However, many simulation studies suggest that the thermal emission is locally likely to be polarized perpendicular to the disc symmetry axis. This is especially true when considering optically-thick disc atmospheres with large optical depth (Dovčiak et al. 2008; Taverna et al. 2020), or when accounting for absorption processes alongside scattering ones (Taverna et al. 2021). The coronal emission polarization vector can be either parallel or perpendicular to the disc axis, depending on the corona geometry, its location, and velocity (see e.g. Zhang et al. 2022). Nevertheless, the recent observation of Cyg X-1 (Krawczynski et al. 2022) as well as theoretical predictions for a flat corona sandwiching the disc (see e.g. Poutanen & Svensson 1996; Schnittman & Krolik 2010; Krawczynski & Beheshtipour 2022) suggest that this component is polarized in the same direction as the disc axis. Hence, we forced the polarization vectors of the two components to be perpendicular to each other. (We also explored the parallel configuration, which is described in Appendix B.) In this configuration, the total polarization degree of the model is given by the difference between the two components' contribution, effectively allowing for two unphysically large polarization degree values at the same time. To avoid this, we restricted our analysis to three reasonable values for the coronal emission polarization degree: 0, 4 (the best-fitting value for coronal emission polarization degree found for Cyg X-1 in Krawczynski et al. 2022), and 10 per cent. The resulting contour plots for the polarization degree and angle of the thermal emission are shown in Fig. 7. The ionization cone orientation of $\sim 45°$ suggests that the projected accretion disc orientation is perpendicular to the jet-remnant direction (see e.g. Krawczynski et al. 2022), i.e. approximately $-45° \pm 22.5°$ in our plots, taking into account the observed opening angle of the ionization cone. Thus the thermal component is expected to be polarized in this direction.

When assuming the coronal emission to be unpolarized, we found an upper limit of 2.3 per cent on the thermal emission polarization degree, while forcing the polarization angle to be directed as the projected accretion plane this value reduces to 0.5 per cent. When taking into account the coronal emission polarization, the contour plots show two minima, representing two allowed configurations. In one case the thermal component is polarized in the same direction as the projected accretion plane with a low polarization degree, while

in the other it is polarized perpendicularly to it, but with a larger polarization degree. In both cases, the polarization degree upper limits tend to increase, becoming as high as $\Pi = 3.4$ and 5.1 per cent when the Comptonized component polarization degree is fixed at 4 and 10 per cent, respectively; and $\Pi = 1.7$ and 3.6 per cent, if we further assume the suggested system orientation. These polarization degree values are all well within the Chandrasekhar estimates for the polarization of thermal radiation. The polarization angle value is unconstrained at the 99 per cent confidence level in all cases, but already at the 90 per cent confidence level the contours indicate that the polarization angle is either perpendicular or parallel to the ionization cone direction (see Fig. 7).

### 3.3.2 *Physical polarization model*

The polarization of the radiation emitted near a black hole is expected to be influenced by the compact object's strong gravitational field (Stark & Connors 1977; Connors & Stark 1977; Connors et al. 1980). Relativistic light bending causes the photons' polarization vectors to rotate as they propagate toward the observer. This results in a net depolarization of the observed radiation when photons' polarization vectors are summed up at infinity. To account for this and other special and general relativity effects on the polarization observables we employed in XSPEC the model `KYNBBRR`. This model is an extension of the relativistic package KYN (Dovčiak et al. 2004, 2008), developed to include the contribution of returning radiation, i.e. photons that are bent by strong gravity effects and forced to return to the disc surface, where they can be reflected before eventually reaching the observer (Schnittman & Krolik 2009; Taverna et al. 2020). We refer to Mikusincova et al. (2023) and references therein for the model theoretical framework.

To implement this model in XSPEC we first focused only on *IXPE I* spectra and froze all parameters of Model 2 to their best-fitting values. Then we replaced `POLCONST * KERRBB` with `KYNBBRR`. We kept the mass, distance, inclination angle, black hole mass and spin fixed at the values used for `KERRBB` in the previous fit. We initially kept the `ALBEDO` parameter (i.e. the fraction of the returning radiation component not absorbed on the disc surface) fixed at 0. We performed this preliminary fit, leaving only the accretion rate and the normalization as free parameters, which resulted in the best-fitting values listed in Table 2 and $\chi^2/\mathrm{dof} = 522.83/447$. With all these parameters set, we extracted from the code the theoretical prediction for the thermal emission polarization degree and angle in the *IXPE* energy range, shown in Fig. 8 for different `ALBEDO` values. Next, we replaced *IXPE I* spectra with the $Q$ and $U$ ones. We employed a `POLCONST` component to model the polarization properties of the coronal emission and left its parameters free to vary in the fit together with the `KYNBBRR` orientation parameter $\chi$, which indicates the accretion disc axis direction. The best-fitting parameter values are listed in Table 2 with fit quality $\chi^2/\mathrm{dof} = 844.15/894$.

We further investigated the polarimetric data by forcing the polarization angle of the Comptonized component to be either perpendicular or parallel to the `KYNBBRR` orientation, as described for the phenomenological model in Section 3.3.1. The `KYNBBRR` orientation was left free to vary in the fit, together with the Comptonized component polarization degree. The contour plots for these two parameters, presented in Fig. 9, show that the orientation of the system was unconstrained in the various fits, also we did not obtain any strong upper limits for the coronal emission polarization degree. This situation did not improve by exploring different values of the `ALBEDO` parameter to account for the returning radiation contribution. It is worth noting that in `KYNBBRR` the thermal emission is expected to be polarized

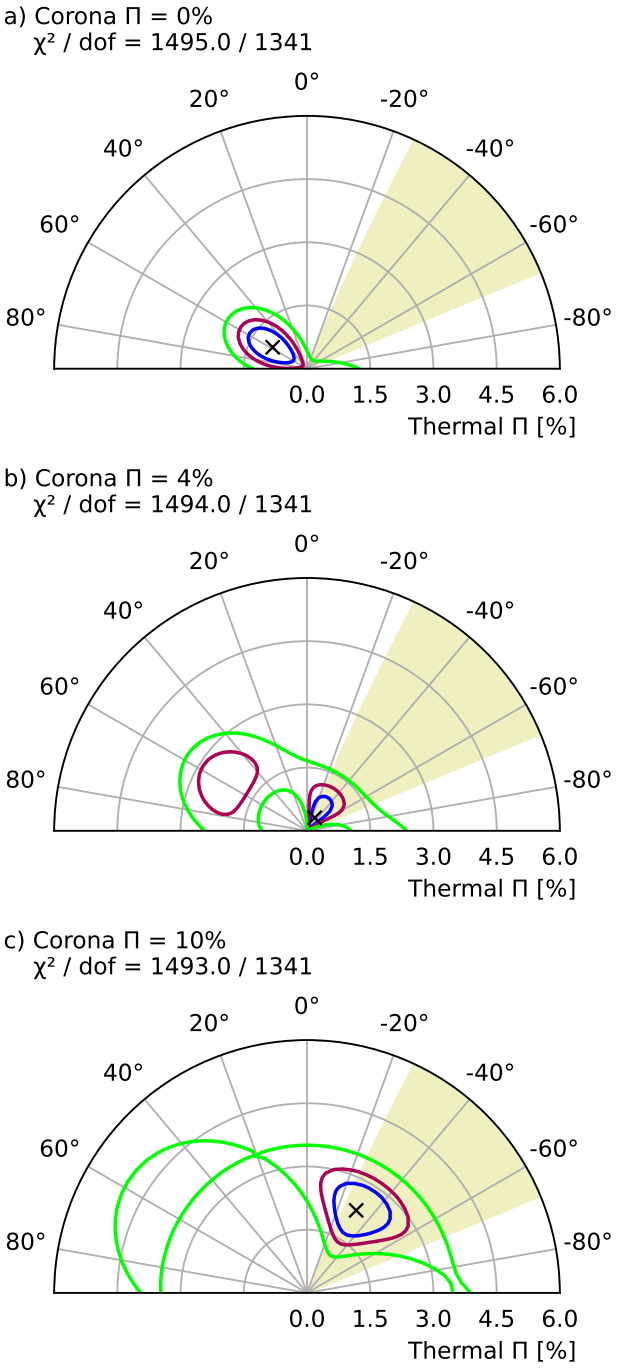


**Figure 7.** Contour plots of the polarization degree $\Pi$ and angle $\Psi$ associated to the accretion disc thermal emission. Blue, red, and green lines indicate 68, 90, and 99 per cent confidence levels for two parameters of interest, respectively. The black cross indicates the best-fit parameters for the $\chi^2/\mathrm{dof}$ value shown in the label. The coronal emission is assumed to be polarized perpendicularly to the thermal component, and its polarization degree is fixed at 0 (*top*), 4 (*middle*), and 10 per cent (*bottom*). The yellow-shaded region indicates the projected accretion disc orientation, perpendicular to the ionization cone. The accretion disc is assumed to be aligned with the orbital inclination $i = 36.4°$ (Orosz et al. 2009).

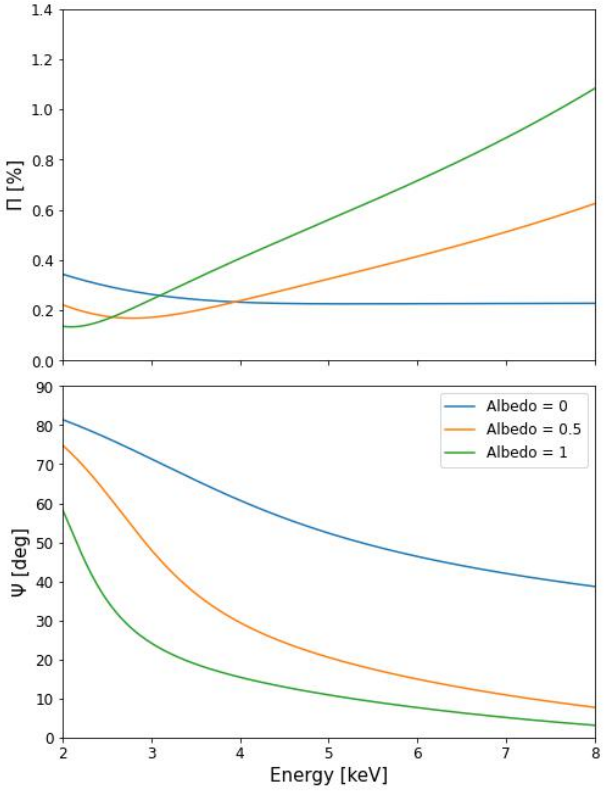


**Figure 8.** Polarization degree (*top*) and angle (*bottom*) predicted by KYNBBRR model for black holes thermal emission in the 2–8 keV energy range, assuming all system parameters fixed at their respective best-fitting values (see Table 2). The different colours indicate different contributions of the returning radiation component, regulated by the albedo parameter. The accretion disc is assumed to be aligned with the orbital inclination $i = 36.4°$ (Orosz et al. 2009). Here, the orientation of the disc axis is assumed to be $\chi = 0°$ for the polarization angle computations.

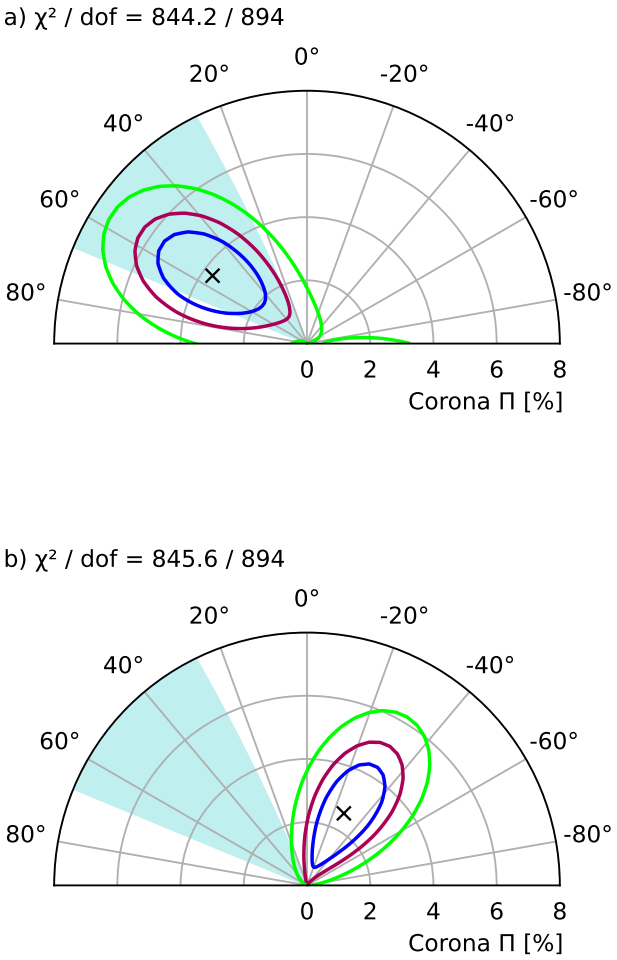


**Figure 9.** Contour plots of the coronal emission polarization degree Π and the KYNBBRR orientation parameter $\chi$. The coronal emission is assumed to be polarized in the same way as the disc axis (*top*) or perpendicularly to it (*bottom*). Blue, red, and green lines indicate 68, 90, and 99 per cent confidence levels for two parameters of interest, respectively. The black cross indicates the best-fit parameters for the $\chi^2$/dof value shown in the label. The cyan-shaded region indicates the ionization cone opening angle (Cooke et al. 2008). The accretion disc is assumed to be aligned with the orbital inclination $i = 36.4°$ (Orosz et al. 2009).

perpendicular to the disc axis before taking into account general relativistic effects. So in the configuration shown in the top panel of Fig. 9, the polarization vectors of the two components are perpendicular to each other, and the model gives an indication for the observed polarization properties to be due to the coronal emission, and to be partially aligned with the source ionization cone (Cooke et al. 2008). On the other hand, in the bottom panel of Fig. 9 the polarization vectors of the two components are parallel with each other and with the accretion disc plane. Thus the system symmetry axis favors directions perpendicular to the ionization cone; configurations where the axis direction is within the ionization cone opening are allowed, but only if the coronal emission polarization degree is below 1 per cent. This statistically less significant scenario is still allowed due to the fact that the *IXPE* observation of this source detected only an upper limit of the polarization degree which allows the polarization angle of the system to be in any direction, i.e. also in the direction perpendicular to the ionization cone.

Because the polarization properties are sensitive to the geometry of the emitting region they can be used to investigate the accretion disc inclination and the black hole spin in black hole binaries (Taverna et al. 2020; Taverna et al. 2021; Mikusincova et al. 2023). For this reason, we further explored the parameter space to check whether it was possible to fit the polarimetric data with different values of these two parameters. For rapidly rotating black holes ($a = 0.92, 0.998$), we found that it was possible to explain the data with an inclination angle as high as 70° even considering the coronal emission as unpolarized (with $i = 70°$, $\chi^2$/dof = 900.78/894 and $\chi^2$/dof = 883.74/894 for $a = 0.92$ and 0.998, respectively). When considering a non-rotating object, the polarization degree predicted for the thermal emission was larger than the detected polarization degree upper limit, however, it was still possible to fit the data by assuming the coronal emission was polarized perpendicular to the thermal emission ($\chi^2$/dof = 885.57/894 for $i = 70°$ and $a = 0$). Thus, although our data are in agreement with a model with a fast-rotating black hole observed at a small inclination angle, we are not able to better constrain the spin and inclination with high statistical significance.

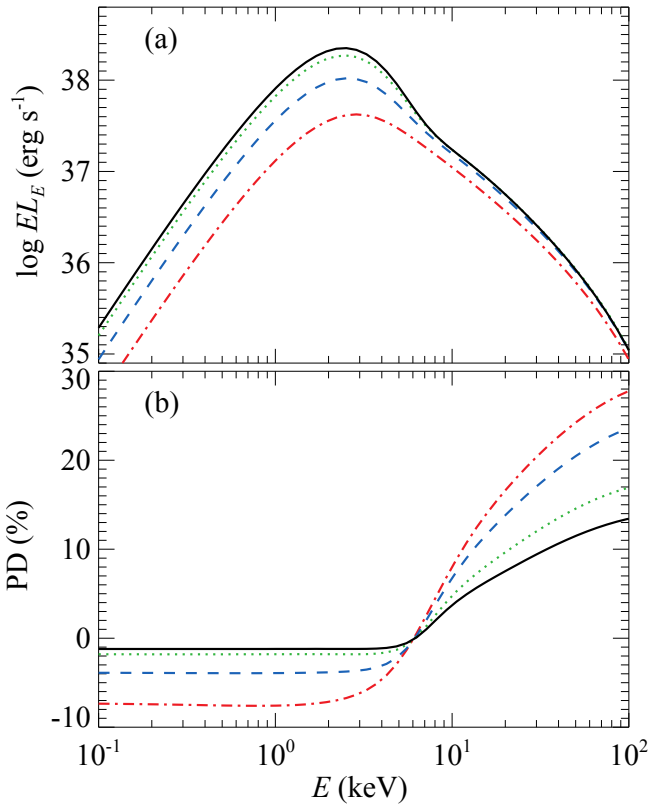


**Figure 10.** Spectral energy distribution (a) and polarization degree (b) obtained for the slab corona model. Lines correspond to different inclinations: $i = 30°$ (black solid), 45° (green dotted), 60° (blue dashed) and 75° (red dot-dashed).

## 4 DISCUSSION

The low polarization of LMC X-1 suggests that the high polarization degree (4 per cent $\lesssim \Pi \lesssim$ 21 per cent, Krawczynski et al. 2022; Veledina et al. 2023) measured for other accreting stellar-mass black holes by *IXPE* might not be a rule, but instead originates in rather specific accretion configurations. The Cyg X-1 measurements in the hard state provided strong evidence for polarization from a dominant coronal component with polarization parallel with the jet (i.e. with the disc axis), excluding many scenarios in the so-called lamp-post coronal geometry. The Cyg X-3 measurements in the hard and intermediate states provided strong evidence for polarization given by a dominant wind-reflection component with polarization parallel with the disc (i.e. perpendicular to the disc axis), while the primary coronal emission was hidden. The observed tight upper limit of 2.2 per cent ($3\sigma$ confidence) on the 2–8 keV polarization of LMC X-1 suggests a mutual mixing of two polarized components oriented perpendicular to each other: the thermal component that is polarized parallel to the disc and consistent with the Chandrasekhar's prescription for a moderately inclined accretion disc, while the Comptonization component is polarized perpendicular to the disc with a higher polarization degree from 1.9 per cent to 5.5 per cent ($1\sigma$ confidence, see Section 3.3.2) consistent with a flat geometry of corona sandwiching the accretion disc.

In addition, we performed simulations of a slab coronal geometry with a cold disc and a hot Comptonization medium above it using a radiative transfer code that splits the radiation field produced by Compton scattering in different orders and computes their intensities, source functions and polarization (Veledina & Poutanen 2022; Poutanen et al. 2023). The code follows the procedures described in Poutanen & Svensson (1996). We assumed the slab is illuminated by the accretion disc whose radiation is described by the single-temperature blackbody $kT_{\rm bb} = 0.6$ keV and angular distribution and polarization follow the Chandrasekhar-Sobolev profile (Chandrasekhar 1960; Sobolev 1963). The temperature of the medium is assumed to be $kT_{\rm e} = 25$ keV. For these conditions, we find that a Thomson optical depth of $\tau_{\rm T} = 0.5$ closely reproduces the observed spectrum for the inclination $i = 30°$. We plot the resulting spectra for different inclinations ($i = 30°, 45°, 60°$ and 75°) in Fig. 10a. In Fig. 10b we show the polarization degree corresponding to this geometry. Positive(/negative) values correspond to polarization parallel(/orthogonal) to the disc axis.

The change of polarization sign at $\sim$ 5 keV is a known feature of the slab corona geometry (see e.g. Poutanen & Svensson 1996), as the sign of each Compton scattering order is controlled by the angular distribution of the incoming (seed) photons. We find that, for the considered parameters, the switch between negative and positive polarization degree occurs in the middle of *IXPE* range. This might be the reason for the low net polarization degree averaged over the entire 2–8 keV band, and can plausibly serve as a mechanism for switching between the positive and negative polarization degrees seen in Fig. 6: variations of the parameters lead to variations of the characteristic energy of zero polarization. In this case, the variations likely have a stochastic, rather than periodic (e.g. at orbital period) origin.

## 5 CONCLUSIONS

We performed a broadband X-ray spectro-polarimetric observational campaign of the black hole binary system LMC X-1 simultaneously with the *IXPE*, *NICER*, *NuSTAR* and ART-XC missions. The spectral data are consistent with previous studies of LMC X-1. We report that the source is in the high/soft state with a dominant thermal component in the X-ray band, a power-law Comptonization component that begins to prevail around $\sim$ 10 keV, and a negligible reflection contribution. The spectra do not show remarkable time variability. The first X-ray polarimetric observation of LMC X-1 by *IXPE* constrains the polarization degree to be below the MDP of 1.1 per cent at the 99 per cent confidence level for the time-averaged emission in the 2–8 keV band. This is consistent with theoretical predictions for pure thermal emission from a geometrically thin and optically thick disc with a Novikov-Thorne profile, assuming Chandrasekhar's prescription for polarization due to scattering in semi-infinite atmospheres. Spectro-polarimetric fitting leads to upper limits on the polarization degree of the thermal radiation to be 0.5, 1.7 or 3.6 per cent when the polarization of power-law component is fixed to 0, 4 or 10 per cent, respectively, if the two components are polarized perpendicular to each other and if we assume a preferred system orientation given by the optical and radio data from literature. The new X-ray polarimetric data show hints of non-zero polarization with the polarization angle aligned with the ionization cone and weak evidence for time variability of the polarization that could be attributed to a stochastic origin in a slab corona scenario sandwiching a thermally radiating accretion disc. Relativistic disc emission models (including returning radiation) provide a 7.7 or 1 per cent polarization upper limit (at 99 per cent confidence level) on the Comptonization component, assuming the two components produce polarization in the directions perpendicular to or parallel with each other, respectively. The 562 ks observation by *IXPE* did not allow statistically significant constraints on the black-hole spin nor the disc inclination.

## ACKNOWLEDGEMENTS

The *Imaging X ray Polarimetry Explorer* (*IXPE*) is a joint US and Italian mission. The US contribution is supported by the National Aeronautics and Space Administration (NASA) and led and managed by its Marshall Space Flight Center (MSFC), with industry partner Ball Aerospace (contract NNM15AA18C). The Italian contribution is supported by the Italian Space Agency (Agenzia Spaziale Italiana, ASI) through contract ASI-OHBI-2017-12-I.0, agreements ASI-INAF-2017-12-H0 and ASI-INFN-2017.13-H0, and its Space Science Data Center (SSDC) with agreements ASI-INAF-2022-14-HH.0 and ASI-INFN 2021-43-HH.0, and by the Istituto Nazionale di Astrofisica (INAF) and the Istituto Nazionale di Fisica Nucleare (INFN) in Italy. This research used data products provided by the *IXPE* Team (MSFC, SSDC, INAF, and INFN) and distributed with additional software tools by the High-Energy Astrophysics Science Archive Research Center (HEASARC), at NASA Goddard Space Flight Center (GSFC).

J.P., M.D., J.S. and V.K. thank for the support from the GACR project 21-06825X and the institutional support from RVO:67985815. A.V. acknowledges support from the Academy of Finland grant 347003. H.K. and N.R.C. acknowledge NASA support under grants 80NSSC18K0264, 80NSSC22K1291, 80NSSC21K1817, and NNX16AC42G. P.O.P. acknowledges financial support from the French High Energy Program (PNHE/CNRS) and from the French spatial agency (CNES). A.I. acknowledges support from the Royal Society.

## DATA AVAILABILITY

The *IXPE* data used in this article are publicly available in the HEASARC database (https://heasarc.gsfc.nasa.gov/docs/ixpe/archive/). The analysis and simulation software IXPEOBSSIM developed by *IXPE* collaboration and its documentation is available publicly through the web-page https://ixpeobssim.readthedocs.io/en/latest/?badge=latest.494. The *NICER* and *NuSTAR* data underlying this article are publicly available from the *NuSTAR* (https://heasarc.gsfc.nasa.gov/docs/nustar/archive/nustar_archive.html) and *NICER* (https://heasarc.gsfc.nasa.gov/docs/nicer/nicer_archive.html) archives. The ART-XC data used in this article publicly available at ftp://hea.iki.rssi.ru/public/SRG/ART-XC/data/LMC_X-1/lmc_x_1_barycen.fits.gz. The XSPEC software is publicly available in the HEASARC database (https://heasarc.gsfc.nasa.gov/xanadu/xspec/). The corresponding XSPEC packages used for this work can be found in the references stated in this article or shared on reasonable request.

## REFERENCES

Alam M. S., Dewangan G. C., Belloni T., Mukherjee D., Jhingan S., 2014, MNRAS, 445, 4259
Arnaud K. A., 1996, in Jacoby G. H., Barnes J., eds, Astr. Soc. Pac. Conf. Ser. Vol. 101, Astronomical Data Analysis Software and Systems V. p. 17
Baldini L., et al., 2022, SoftwareX, 19, 101194
Belczynski K., Bulik T., Fryer C. L., 2012, arXiv e-prints, p. arXiv:1208.2422
Belczynski K., Done C., Lasota J. P., 2021, arXiv e-prints, p. arXiv:2111.09401
Bhuvana G. R., Radhika D., Agrawal V. K., Mandal S., Nandi A., 2021, MNRAS, 501, 5457
Bhuvana G. R., Radhika D., Nandi A., 2022, Advances in Space Research, 69, 483
Casella P., Belloni T., Stella L., 2005, ApJ, 629, 403
Chandrasekhar S., 1960, Radiative Transfer. Dover Publications, New York
Cheng Y., Liu D., Nampalliwar S., Bambi C., 2016, Classical and Quantum Gravity, 33, 125015
Connors P. A., Stark R. F., 1977, Nature, 269, 128
Connors P. A., Piran T., Stark R. F., 1980, ApJ, 235, 224
Cooke R., Kuncic Z., Sharp R., Bland-Hawthorn J., 2007, ApJ, 667, L163
Cooke R., Bland-Hawthorn J., Sharp R., Kuncic Z., 2008, ApJ, 687, L29
Di Marco A., et al., 2022, AJ, 163, 170
Dovčiak M., Karas V., Matt G., 2004, MNRAS, 355, 1005
Dovčiak M., Muleri F., Goosmann R. W., Karas V., Matt G., 2008, MNRAS, 391, 32
Ebisawa K., Mitsuda K., Inoue H., 1989, PASJ, 41, 519
Fabian A. C., Rees M. J., Stella L., White N. E., 1989, MNRAS, 238, 729
Fender R., 2006, in , Vol. 39, Compact stellar X-ray sources. pp 381–419
Fishbach M., Kalogera V., 2022, ApJ, 929, L26
Gendreau K. C., Arzoumanian Z., Okajima T., 2012, in Takahashi T., Murray S. S., den Herder J.-W. A., eds, Society of Photo-Optical Instrumentation Engineers (SPIE) Conference Series Vol. 8443, Space Telescopes and Instrumentation 2012: Ultraviolet to Gamma Ray. p. 844313, doi:10.1117/12.926396
Gierliński M., Maciołek-Niedźwiecki A., Ebisawa K., 2001, MNRAS, 325, 1253
Gou L., et al., 2009, ApJ, 701, 1076
Hanke M., Wilms J., Nowak M. A., Barragán L., Schulz N. S., 2010, A&A, 509, L8
Harrison F. A., et al., 2013, ApJ, 770, 103
Heasarc 2014, HEAsoft: Unified Release of FTOOLS and XANADU, Astrophysics Source Code Library, record ascl:1408.004 (ascl:1408.004)
Hughes A., Staveley-Smith L., Kim S., Wolleben M., Filipović M., 2007, MNRAS, 382, 543
Hyde E. A., Russell D. M., Ritter A., Filipović M. D., Kaper L., Grieve K., O'Brien A. N., 2017, PASP, 129, 094201
Jana A., Naik S., Chatterjee D., Jaisawal G. K., 2021, MNRAS, 507, 4779
Kaastra J. S., Bleeker J. A. M., 2016, A&A, 587, A151
Kislat F., Clark B., Beilicke M., Krawczynski H., 2015, Astroparticle Physics, 68, 45
Koyama S., Yamada S., Kubota A., Tashiro M. S., Terada Y., Makishima K., 2015, PASJ, 67, 46
Krawczynski H., Beheshtipour B., 2022, ApJ, 934, 4
Krawczynski H., et al., 2022, Science, 378, 650
Kubota A., Ebisawa K., Makishima K., Nakazawa K., 2005, ApJ, 631, 1062
Levine A. M., Bradt H., Cui W., Jernigan J. G., Morgan E. H., Remillard R., Shirey R. E., Smith D. A., 1996, ApJ, 469, L33
Levine A. M., Bradt H. V., Chakrabarty D., Corbet R. H. D., Harris R. J., 2011, ApJS, 196, 6
Li L.-X., Zimmerman E. R., Narayan R., McClintock J. E., 2005, ApJS, 157, 335
Li L.-X., Narayan R., McClintock J. E., 2009, ApJ, 691, 847
Madsen K. K., Forster K., Grefenstette B. W., Harrison F. A., Stern D., 2017, ApJ, 841, 56
Marinucci A., et al., 2022, MNRAS, 516, 5907
Mark H., Price R., Rodrigues R., Seward F. D., Swift C. D., 1969, ApJ, 155, L143
Matsuoka M., et al., 2009, PASJ, 61, 999
Mehta V. M., Demirtas M., Long C., Marsh D. J. E., McAllister L., Stott M. J., 2021, J. Cosmology Astropart. Phys., 2021, 033
Mikusincova R., Dovciak M., Bursa M., Lalla N. D., Matt G., Svoboda J., Taverna R., Zhang W., 2023, MNRAS, 519, 6138
Mudambi S. P., Rao A., Gudennavar S. B., Misra R., Bubbly S. G., 2020, MNRAS, 498, 4404
Novikov D. I., Thorne K. S., 1973, in Witt B., Witt C., eds, Les Astres Occlus. Gordon & Breach, New York, p. 343
Nowak M. A., Wilms J., Heindl W. A., Pottschmidt K., Dove J. B., Begelman M. C., 2001, MNRAS, 320, 316
Orosz J. A., et al., 2007, Nature, 449, 872
Orosz J. A., et al., 2009, ApJ, 697, 573
Pakull M. W., Angebault L. P., 1986, Nature, 322, 511

Pavlinsky M., et al., 2021, A&A, 650, A42
Podsiadlowski P., Rappaport S., Han Z., 2003, MNRAS, 341, 385
Poutanen J., Svensson R., 1996, ApJ, 470, 249
Poutanen J., Veledina A., Beloborodov A. M., 2023, ApJ, submitted, p. arXiv:2302.11674
Qin Y., Marchant P., Fragos T., Meynet G., Kalogera V., 2019, ApJ, 870, L18
Remillard R. A., McClintock J. E., 2006, ARA&A, 44, 49
Remillard R. A., et al., 2022, AJ, 163, 130
Schmidtke P. C., Ponder A. L., Cowley A. P., 1999, AJ, 117, 1292
Schnittman J. D., Krolik J. H., 2009, ApJ, 701, 1175
Schnittman J. D., Krolik J. H., 2010, ApJ, 712, 908
Shakura N. I., Sunyaev R. A., 1973, A&A, 500, 33
Shao Y., Li X.-D., 2022, ApJ, 930, 26
Sobolev V. V., 1963, A treatise on radiative transfer. Princeton: Van Nostrand
Stark R. F., Connors P. A., 1977, Nature, 266, 429
Steiner J. F., et al., 2011, MNRAS, 416, 941
Steiner J. F., et al., 2012, MNRAS, 427, 2552
Strohmayer T. E., 2017, ApJ, 838, 72
Sunyaev R. A., Titarchuk L. G., 1980, A&A, 86, 121
Sunyaev R., et al., 2021, A&A, 656, A132
Taverna R., Zhang W., Dovčiak M., Bianchi S., Bursa M., Karas V., Matt G., 2020, MNRAS, 493, 4960
Taverna R., Marra L., Bianchi S., Dovčiak M., Goosmann R., Marin F., Matt G., Zhang W., 2021, MNRAS, 501, 3393
Tripathi A., et al., 2020, ApJ, 897, 84
Ursini F., et al., 2023, MNRAS, 519, 50
Veledina A., Poutanen J., 2022, Polarization of Comptonized emission in slab geometry, doi:10.5281/zenodo.7116125
Veledina A., et al., 2023, arXiv e-prints, p. arXiv:2303.01174
Weisskopf M. C., et al., 2022, Journal of Astronomical Telescopes, Instruments, and Systems, 8, 026002
Wilms J., Allen A., McCray R., 2000, ApJ, 542, 914
Wilms J., Nowak M. A., Pottschmidt K., Heindl W. A., Dove J. B., Begelman M. C., 2001, MNRAS, 320, 327
Zdziarski A. A., Gierliński M., 2004, Progr. Theor. Phys. Suppl., 155, 99
Zdziarski A. A., Johnson W. N., Magdziarz P., 1996, MNRAS, 283, 193
Zhang W., Dovčiak M., Bursa M., 2019, ApJ, 875, 148
Zhang W., Dovčiak M., Bursa M., Karas V., Matt G., Ursini F., 2022, MNRAS, 515, 2882
Życki P. T., Done C., Smith D. A., 1999, MNRAS, 309, 561

## APPENDIX A: OBSERVATIONS AND DATA REDUCTION OF *NICER*, *NUSTAR* AND ART-XC

In Section 2 we already described in detail the *IXPE* data reduction. For completeness, we also show in Fig. A1 the *IXPE* count maps indicating the regions chosen to select the source and the background in the field of view.

We now return to the other three instruments forming the observational campaign. *NICER* (Gendreau et al. 2012) is a soft X-ray spectral-timing instrument aboard the International Space Station, sensitive within ∼ 0.2–12 keV band. It is non-imaging, and composed of 56 silicon-drift detectors, each of which is paired with a concentrator optic, commonly aligned to a single field approximately 3′ in radius. 52 detectors have been active since launch, although in any given observation, some detectors may be temporarily disabled. *NICER* observed LMC X-1 during the course of the *IXPE* observational campaign, for a total of 13.5 ks *useful* time among 10 ObsIDs from 2022 October 19–28.

*NICER* data were reduced using NICERL2 with unrestricted undershoot and overshoot rates. The background was computed using the "3C50" model (Remillard et al. 2022). Subsequently, the data were filtered to remove intervals with background count rates more than 1 per cent the source rate, and any short GTI intervals <60s were removed. For each observation, the detectors were screened for outliers in overshoot or undershoot event rates which are generated by particle background and optical-loading events, respectively. For both fields, each detector was compared to the detector distribution, and those more than $10\sigma$ equivalent from the median were filtered out. *NICER* spectra were rebinned in order to oversample the instrumental energy resolution by a factor ∼ 3. *NICER* observations were found to be relatively constant in flux and consistent in spectral properties over the *IXPE* campaign, and with low power-density rms noise.

The *NuSTAR* spacecraft (Harrison et al. 2013) acquired a total of 19 ksec of data on 2022 October 24 under observation ID 90801324002. The *NuSTAR* data were processed with the `NuSTARDAS` software (version 2.1.1) of the `HEAsoft` package (version 6.29) (Heasarc 2014). Source and background events were selected with a circular region of ∼ 67 arcsec radii for both focal plane modules (FPMA/FPMB). `FTGROUPPHA` was used to rebin the spectra implementing the Kaastra & Bleeker (2016) optimal binning scheme.

We note that we used the cross-calibration model `MBPO` employed in Krawczynski et al. (2022) to reconcile discrepancies between the instruments when performing the joint fits in Sections 3.1 and 3.3 with the *NICER*, *NuSTAR* and *IXPE* spectra. For the first of the 10 *NICER* observations, we fixed the power-law indices in the `MBPO` model to zero and the normalization to one to establish a comparison between observations and instruments. The normalization parameter of each of the remaining *NICER* observations are allowed to vary.[2] For the *NuSTAR* FPMs, the high and low energy power-law indices are tied and allowed to vary together with the normalization parameter.[3] For the *IXPE* detector units, all parameters in `MBPO` are allowed to vary freely.[4] We also included a 0.5 per cent systematic uncertainty to all instruments used in the data analysis apart from *NICER*, where we accounted for 1.5 per cent systematic uncertainty, according to the mission's recommendation.[5] This is necessary to take into account the unknown internal calibration.

We deal with the absolute flux uncertainty associated with X-ray detectors by initially arbitrarily assuming the first *NICER* observation to be correctly calibrated (i.e. we fix the norm of the `MBPO` cross-calibration model to be unity; see above), and allowing the calibration constants for the other observatories and the normalization of the `KERRBB` model to be free parameters. Our best fitting value for the `KERRBB` normalization is ∼ 0.74 (see Table 1). If we had instead frozen the `KERRBB` normalization to unity (as should physically be the case) and let all calibration constants be free, we would have found a fit of identical quality with calibration constant ∼ 0.74 for the first *NICER* observation and ∼ 0.76 for the *NuSTAR* FPMs. *NuSTAR* has the best absolute flux calibration of the instruments

[2] For the fit presented in Table 1 we obtained the normalization values of 1.0184±0.0039, 0.9622±0.0034, 1.1624±0.0072, 1.0897±0.0037, 1.0994±0.0037, 1.1372±0.0038, 1.0739±0.0035, 0.9824±0.0039, 0.9992±0.0038, for the *NICER* observations 2–10, respectively.

[3] For the fit presented in Table 1 we obtained the $\Delta\Gamma_1$ values of $0.056 \pm 0.012$ and $0.052 \pm 0.012$, and the normalization values of $1.0264 \pm 0.0078$ and $1.0241 \pm 0.0080$, for the *NuSTAR* focal plane modules FPMA and FPMB, respectively.

[4] For the fit presented in Table 1 we obtained the $\Delta\Gamma_1$ values of $-0.1418 \pm 0.0062$, $-0.1007 \pm 0.0064$, $-0.0924 \pm 0.0065$, the $\Delta\Gamma_2$ values of $0.66 \pm 0.36$, $0.16 \pm 0.39$, $0.84 \pm 0.33$, the $E_{\rm br}$ values of $6.31 \pm 0.24$, $6.57 \pm 0.96$, $6.43 \pm 0.24$, and the normalization values of $0.8891 \pm 0.0049$, $0.8855 \pm 0.0132$, $0.8477 \pm 0.0031$, for the *IXPE* DUs 1, 2, 3, respectively.

[5] Available at `https://heasarc.gsfc.nasa.gov/docs/nicer/analysis_threads/cal-recommend/`.

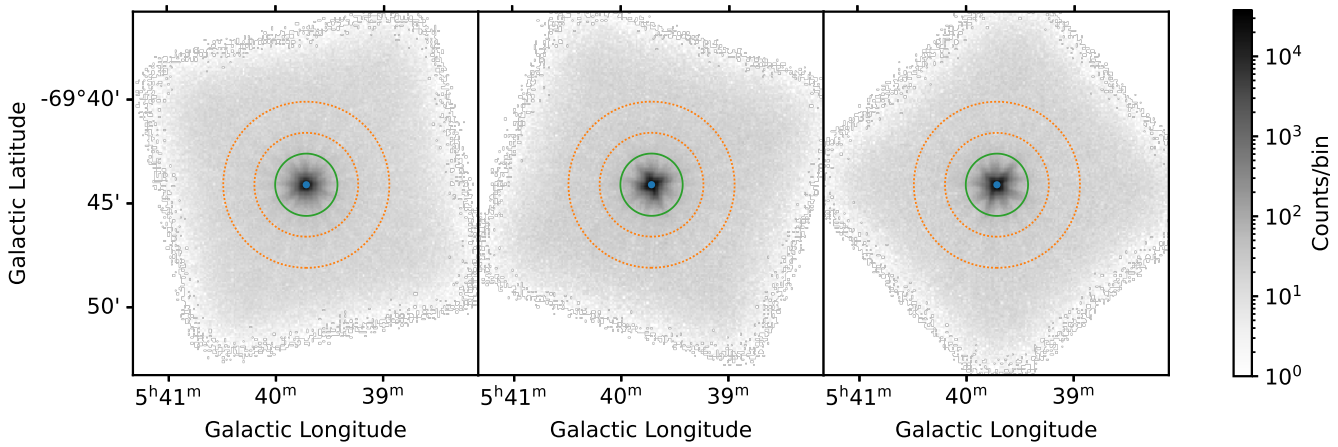


**Figure A1.** Count maps of the three *IXPE* telescopes. The scale of the colour bar is logarithmic to make visible, in addition to the source, also the much fainter background. The regions used to angularly select the source and background in the field of view are the green solid circle and the dashed orange annulus, respectively.

considered here, and a calibration constant of ∼ 0.76 is only ∼ 13% smaller than the recommended value of ∼ 0.87 derived from unfocused observations of the Crab Nebula (Madsen et al. 2017). Such a discrepancy is comparable to the ∼ 10% systematic routinely assumed on the absolute flux calibration when fitting disc models (e.g. Steiner et al. 2011).

The Mikhail Pavlinsky ART-XC telescope is a grazing incidence focusing X-ray telescope (Pavlinsky et al. 2021) on board the *Spectrum-Rontgen-Gamma observatory* (*SRG*, Sunyaev et al. 2021). It observed LMC X-1 on 2022 Oct 27 with a total exposure of 84.4 ks. The ART-XC observation has two short technical interruptions of ∼ 100 s duration each. ART-XC data were processed with the analysis software `ARTPRODUCTSv1.0` and the `CALDB` (calibration data base) version 20220908.

## APPENDIX B: PARALLEL CONFIGURATION OF THE TWO SPECTRAL COMPONENTS POLARIZATION VECTORS

In the main part of this paper, we considered the thermal and the coronal emission to be polarized perpendicularly to each other. However, since both components' polarization vectors can be either parallel or perpendicular to the disc axis, we cannot exclude the opposite configuration. So we performed the analysis described in Section 3.3 also assuming the two components as polarized in the same direction. The contour plots for the thermal emission $\Pi$ and $\Psi$ are shown in Fig. B1. In this case, the two components polarization vector must be added to obtain the observed one; this means that as the coronal emission polarization degree increases we get better constraints on the thermal emission polarization properties. This effect is particularly interesting regarding the thermal emission polarization angle: assuming the coronal emission to be polarized for at least 4 per cent we can give an estimate of its value of $\Psi = 58° \pm 26°$, partially aligned with the ionization cone observed in the source (Cooke et al. 2007; Cooke et al. 2008). If we assume the thermal emission to be polarized perpendicularly to the disc axis (Dovčiak et al. 2008; Taverna et al. 2020; Taverna et al. 2021), we get that the jet direction should be perpendicular to the ionization cone. The accretion disc emission polarization degree upper limit decreases to 1 and 0.3 per cent for the coronal emission polarization degree of 4 and 10 per cent, respectively.

## AUTHORS' AFFILIATIONS

[1] Université de Strasbourg, CNRS, Observatoire Astronomique de Strasbourg, UMR 7550, 67000 Strasbourg, France
[2] Astronomical Institute of the Czech Academy of Sciences, Boční II 1401/1, 14100 Praha 4, Czech Republic
[3] Astronomical Institute, Charles University, V Holešovičkách 2, CZ-18000 Prague, Czech Republic
[4] Dipartimento di Matematica e Fisica, Università degli Studi Roma Tre, Via della Vasca Navale 84, 00146 Roma, Italy
[5] INAF Istituto di Astrofisica e Planetologia Spaziali, Via del Fosso del Cavaliere 100, I-00133 Roma, Italy
[6] Physics Department and McDonnell Center for the Space Sciences, Washington University in St. Louis, St. Louis, MO 63130, USA
[7] Center for Astrophysics | Harvard & Smithsonian, 60 Garden St, Cambridge, MA 02138, USA
[8] Department of Physics and Astronomy, FI-20014 University of Turku, Finland
[9] Nordita, KTH Royal Institute of Technology and Stockholm University, Hannes Alfvéns väg 12, SE-10691 Stockholm, Sweden
[10] NASA Marshall Space Flight Center, Huntsville, AL 35812, USA
[11] California Institute of Technology, Pasadena, CA 91125, USA
[12] Université Grenoble Alpes, CNRS, IPAG, 38000 Grenoble, France
[13] Space Research Institute of the Russian Academy of Sciences, Profsoyuznaya Str. 84/32, Moscow 117997, Russia
[14] Department of Astronomy, University of Maryland, College Park, Maryland 20742, USA
[15] Center for Research and Exploration in Space Science and Technology, NASA/GSFC, Greenbelt, MD 20771, USA
[16] School of Mathematics, Statistics, and Physics, Newcastle University, Newcastle upon Tyne NE1 7RU, UK
[17] Hiroshima Astrophysical Science Center, Hiroshima University, 1- 3-1 Kagamiyama, Higashi-Hiroshima, Hiroshima 739-8526, Japan
[18] Dipartimento di Fisica, Università degli Studi di Roma "Tor Vergata", Via della Ricerca Scientifica 1, I-00133 Roma, Italy
[19] Istituto Nazionale di Fisica Nucleare, Sezione di Roma "Tor Vergata", Via della Ricerca Scientifica 1, 00133 Roma, Italy
[20] Mullard Space Science Laboratory, University College London, Holmbury St Mary, Dorking, Surrey RH5 6NT, UK
[21] Instituto de Astrofísica de Andalucía—CSIC, Glorieta de la Astronomía s/n, 18008 Granada, Spain

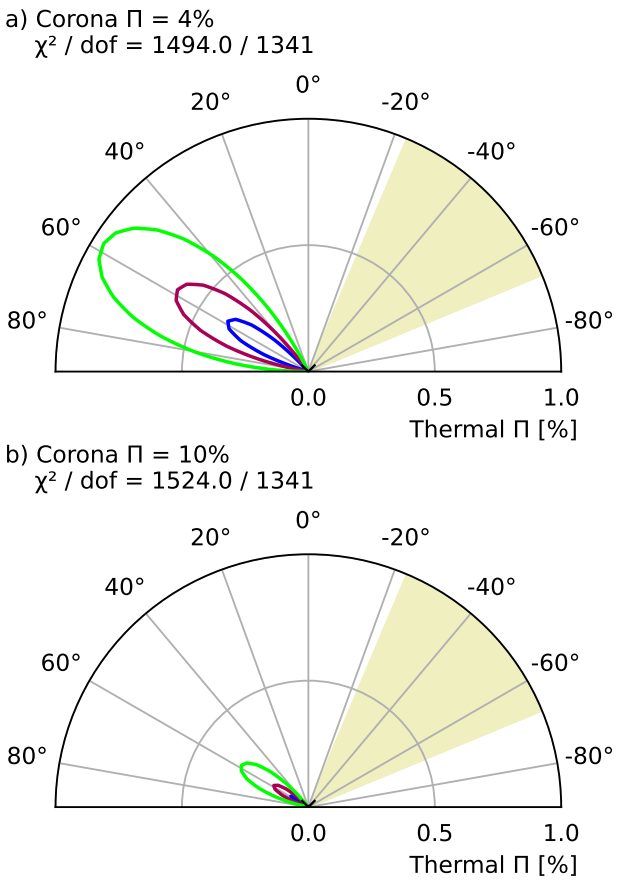


**Figure B1.** Contour plots between the polarization degree Π and angle Ψ associated to the accretion disc thermal emission. Blue, red, and green lines indicate 68 per cent, 90 per cent, and 99 per cent confidence levels for two parameters of interest, respectively. The black cross indicates the best-fit parameters for the $\chi^2$/dof value shown in the label. The coronal emission is assumed to be polarized in the same direction as the thermal component, and its polarization degree is fixed at 4 per cent (*top*) and 10 per cent (*bottom*). The yellow-shaded region indicates the projected accretion disc orientation, perpendicular to the ionization cone. The accretion disc is assumed to be aligned with the orbital inclination $i = 36.4°$ (Orosz et al. 2009).

[22] INAF Osservatorio Astronomico di Roma, Via Frascati 33, 00078 Monte Porzio Catone (RM), Italy
[23] Space Science Data Center, Agenzia Spaziale Italiana, Via del Politecnico snc, 00133 Roma, Italy
[24] INAF Osservatorio Astronomico di Cagliari, Via della Scienza 5, 09047 Selargius (CA), Italy
[25] Istituto Nazionale di Fisica Nucleare, Sezione di Pisa, Largo B. Pontecorvo 3, 56127 Pisa, Italy
[26] Dipartimento di Fisica, Università di Pisa, Largo B. Pontecorvo 3, 56127 Pisa, Italy
[27] Istituto Nazionale di Fisica Nucleare, Sezione di Torino, Via Pietro Giuria 1, 10125 Torino, Italy
[28] Dipartimento di Fisica, Università degli Studi di Torino, Via Pietro Giuria 1, 10125 Torino, Italy
[29] INAF Osservatorio Astrofisico di Arcetri, Largo Enrico Fermi 5, 50125 Firenze, Italy
[30] Dipartimento di Fisica e Astronomia, Università degli Studi di Firenze, Via Sansone 1, 50019 Sesto Fiorentino (FI), Italy
[31] Istituto Nazionale di Fisica Nucleare, Sezione di Firenze, Via Sansone 1, 50019 Sesto Fiorentino (FI), Italy
[32] ASI - Agenzia Spaziale Italiana, Via del Politecnico snc, 00133 Roma, Italy
[33] Science and Technology Institute, Universities Space Research Association, Huntsville, AL 35805, USA
[34] Department of Physics and Kavli Institute for Particle Astrophysics and Cosmology, Stanford University, Stanford, California 94305, USA
[35] Institut für Astronomie und Astrophysik, Universität Tübingen, Sand 1, 72076 Tübingen, Germany
[36] RIKEN Cluster for Pioneering Research, 2-1 Hirosawa, Wako, Saitama 351-0198, Japan
[37] Yamagata University, 1-4-12 Kojirakawamachi, Yamagatashi 990-8560, Japan
[38] Osaka University, 1-1 Yamadaoka, Suita, Osaka 565-0871, Japan
[39] University of British Columbia, Vancouver, BC V6T 1Z4, Canada
[40] International Center for Hadron Astrophysics, Chiba University, Chiba 263-8522, Japan
[41] Institute for Astrophysical Research, Boston University, 725 Commonwealth Avenue, Boston, MA 02215, USA
[42] Department of Astrophysics, St. Petersburg State University, Universitetsky pr. 28, Petrodvoretz, 198504 St. Petersburg, Russia
[43] Department of Physics and Astronomy and Space Science Center, University of New Hampshire, Durham, NH 03824, USA
[44] Finnish Centre for Astronomy with ESO, 20014 University of Turku, Finland
[45] Istituto Nazionale di Fisica Nucleare, Sezione di Napoli, Strada Comunale Cinthia, 80126 Napoli, Italy
[46] MIT Kavli Institute for Astrophysics and Space Research, Massachusetts Institute of Technology, 77 Massachusetts Avenue, Cambridge, MA 02139, USA
[47] Graduate School of Science, Division of Particle and Astrophysical Science, Nagoya University, Furocho, Chikusaku, Nagoya, Aichi 464-8602, Japan
[48] Department of Physics, The University of Hong Kong, Pokfulam, Hong Kong
[49] Department of Astronomy and Astrophysics, Pennsylvania State University, University Park, PA 16802, USA
[50] INAF Osservatorio Astronomico di Brera, Via E. Bianchi 46, 23807 Merate (LC), Italy
[51] Dipartimento di Fisica e Astronomia, Università degli Studi di Padova, Via Marzolo 8, 35131 Padova, Italy
[52] Anton Pannekoek Institute for Astronomy & GRAPPA, University of Amsterdam, Science Park 904, 1098 XH Amsterdam, The Netherlands
[53] Guangxi Key Laboratory for Relativistic Astrophysics, School of Physical Science and Technology, Guangxi University, Nanning 530004, China

This paper has been typeset from a TEX/LATEX file prepared by the author.